Hybrid Advances 11 (2025) 100568

Contents lists available at ScienceDirect

Hybrid Advances

journal homepage: www.journals.elsevier.com/hybrid-advances

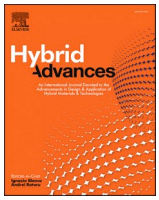

Research Article

Tailoring the synthesis, structural, thermal, magnetic and morphological properties of $Cu_{0.9}Cr_{0.1}Fe_{2-x}Co_xO_4$ (x = 0.1–0.2) spinel ferrites by the substitution of cobalt ions using sol-gel method

Yusuf Sani [a,c], Raba'ah Syahidah Azis [a,b,*], Ismayadi Ismail [a], Yazid Yaakob [b]

[a] Materials Synthesis and Characterization Laboratory (MSCL), Institute of Nanoscience and Nanotechnology (IONS), Universiti Putra Malaysia, UPM Serdang, 43400, Selangor, Malaysia
[b] Department of Physics, Faculty of Science, Universiti Putra Malaysia, UPM, 43400, Serdang, Selangor Darul Ehsan, Malaysia
[c] Department of Pure and Applied Physics, Federal University Wukari, P.M.B 1020, Wukari, Taraba state, Nigeria

ARTICLE INFO

Keywords:
Spinel Ferrite
Nanoparticle
Sol-gel
FTIR
And Magnetic materials

ABSTRACT

This study effectively modifies the structural, thermal, magnetic, and morphological characteristics of $Cu_{0.9}Cr_{0.1}Fe_{2-x}Co_xO_4$ (x = 0.1–0.2) nano-structured spinel ferrites by substituting Co^{2+} ions. The materials were synthesized using the sol-gel auto-combustion process, and they were characterized using XRD, TGA-DTA, RAMAN, FTIR, VSM, FESEM, and HRTEM investigations. The existence of a single-phase spinel nanostructure devoid of secondary phases was verified by the XRD data. The impact of Co^{2+} ions on crystallite size, grain size, and lattice constant was analyzed, revealing that the lattice constant increased with a Co^{2+} ion concentration of x = 0.2. FTIR results showed two absorption bands at $V_1 = 1641\ cm^{-1}$ and $V_2 = 3413\ cm^{-1}$, corresponding to ions moving from tetrahedral to octahedral sites in the spinel structure. VSM analysis revealed the soft magnetic behavior of all samples, with Co^{2+} substitution, the coercivity shows a rising trend **by 2.25** %, which is associated with the significant magnetic anisotropy feature of Co^{2+} species in B sites. At room temperature, cobalt improves the material's ferromagnetic properties, as seen by the 4.6 % improvement in saturation magnetization. These benefits may spark a lot of interest in using this ferrite in loudspeakers, sensors, memory, high-density data storage devices and high-density magnetic recording, among other applications.

1. Introduction

Ferrites are fascinating for both fundamental study and real-world applications because of their exceptional physical, chemical, and magnetic properties. AB_2O_4 is the typical formula for spinel ferrites. Cations occupy tetrahedral (A-sites) and octahedral (B-sites) interstices in the spinel ferrite structure, which is based on a tightly packed oxygen lattice. Compounds containing divalent ions mostly in octahedral sites are referred to as inverse, cwhereas spinel's with divalent ions solely in tetrahedral positions are considered normal. The interactions between cations in the tetrahedral (A-sites) and octahedral (B-sites) are primarily responsible for the intriguing characteristics of spinel ferrites [1,2]. Numerous chemical processes are well known for creating ultrafine ferrite powders, such as sol-gel synthesis [3], co-precipitation techniques [4], and hydrothermal synthesis approaches [5,6]. The sol-gel approach stands out among these methods due to its ability to produce a substantial amount of compositional homogeneity at a very low temperature in a brief processing period [7]. As a result, ferrites may be used for a variety of purposes, such as storage heads, loading coils, antenna rods, electricity transformers, microwave components, computer memory, logical devices, hyperthermia, and colour monitoring tubes [8,9].

$Cu_{0.9}Cr_{0.1}Fe_{2-x}Co_xO_4$ ferrites are among the finest magnetic materials for researchers because of their special qualities, which include low coercivity, low eddy current, minimal dielectric losses, excellent electric resistivity, Curie temperature, cheap cost, and improved environmental stability [10]. $Cu_{0.9}Cr_{0.1}Fe_{2-x}Co_xO_4$, a cobalt-substituted copper-chromium ferrite, has various applications in magnetic materials due to its unique properties [11]. It may be used in information storage devices where stability and strong magnetic coercivity are essential, such as

This article is part of a special issue entitled: HMT-Research Articles published in Hybrid Advances.

* Corresponding author. Department of Physics, faculty of Science, Universiti Putra Malaysia, UPM, Serdang, Selangor Darul Ehsan, 43400, Malaysia.
E-mail address: rabaah@upm.edu.my (R.S. Azis).

https://doi.org/10.1016/j.hybadv.2025.100568
Received 8 July 2025; Received in revised form 28 September 2025; Accepted 17 October 2025
Available online 17 October 2025

magnetic tapes and hard disc drives [12]. Its magnetic properties make it suitable for transformers and inductors, which require high magnetic permeability and low losses [13]. Additionally, Cu–Cr ferrites are effective for EMI shielding to protect electronic devices from interference. They are also used in magnetic sensors for automotive, industrial, and consumer electronics to detect magnetic fields and convert them into electrical signals, ferrofluid technology, sensor technology [14]. Furthermore, this material can absorb microwave radiation, making it useful in radar and communication systems. Lastly, Cu–Cr ferrites have potential in environmental catalysis for reducing pollutants. Panwar et al. (2024) used the sol-gel method approach to successfully manufacture $Ca_{1-x}Bi_xFe_{12-x}Co_xO_{19}$ ferrite. The samples' XRD patterns show that the peaks closely resemble the typical M-type hexaferrite patterns. According to magnetic analysis, conductivity is caused by polaron hopping at higher temperatures and impurities at room temperature. The dielectric material has a heterogeneous structure divided by very resilient thin grain boundaries, according to the Maxwell–Wagner model [15]. When novel synthesis processes improve the performance of current materials or new materials are discovered with improved qualities, researchers are constantly interested, especially when these developments are affordable. Therefore, our goal has been to improve the inherent characteristics of Cu–Cr ferrite by gradually increasing the replacement of Co^{3+} ions using the sol-gel technique. The incorporation of various metal ions into spinel ferrites may drastically change their electric and magnetic characteristics. For example, by simply replacing Cr ions in AB_2O_4, it is possible to regulate critical magnetic characteristics like remanence and coercivity due to their antiferromagnetic nature, which results in the creation of technologically significant materials [16]. Hashim et al. (2012) synthesized Co–Cu ferrite nanoparticles using the sol-gel technique. The result shows that studies of magnetic hysteresis at ambient temperature showed a reduction in saturation magnetization with Cu doping, which could be because Cu and Fe ions have different magnetic moments. The one-phase cubic spinel shape generated by copper-doped cobalt ferrite was confirmed by FTIR and XRD analysis [17]. Calero et al. (2007) synthesized cobalt-substituted ferrite ($Co_xFe_{3-x}O_4$) nanomaterials using reverse micelle techniques. The FTIR measurements showed bands characteristic of the metal–oxygen link in ferrites. With a lattice parameter that is similar to that of $CoFe_2O_4$. Gupta and Sahni (2024) synthesized nanoscale spinel $CoFe_2O_4$ ferrite particles using the sol–gel method, resulting in a single-phase cubic spinel structure with an average crystallite size of 37.18 nm and particle size distribution ranging between 30 and 40 nm. The interplanar spacing was 0.2735 nm, confirming the ferrite's structural integrity. Magnetic characterization confirmed the sample's cation distribution and compositional characteristics [18].

Designing new magnetic materials requires an understanding of the connection between particle size, structure, and magnetic properties. Investigating the effects of Co^{2+} ion concentration on the magnetic, structural, thermal, and morphological properties of Cu–Cr nanoferrite particles produced using the sol-gel technique is the primary objective of this work.

Cobalt ferrite has also been investigated for use in several developing sectors, including biomedicine, catalysis, permanent magnets, and sensors. The substitution of cobalt ions into the ferrite lattice can significantly influence their structural, magnetic, electrical, and catalytic behaviors. Suresh et al. (2021) reported that the incorporation of Co and Cu co-doped Ni-ferrite nanocrystals made the photocatalytic degradation of crystal violet dye more effective when it was exposed to sunlight, with a degradation rate of about 94.14 %. This improvement is attributed to co-doping's increased surface area and decreased bandgap energy, which promote improved charge carrier stabilization and greater photocatalytic activity [19].

Researchers are exploring the use of cobalt ferrite nanostructures as permanent magnets due to their good coercivity and lightweight properties. This has led to increased interest in their magnetic properties, as they have applications in various technological fields such as strong magnets, magnetic fluids, drug delivery, microwave devices, and high-density information storage [6]. Additionally, by substituting cations, these materials' electrical resistivity may be modified, which is advantageous for use in microwave devices and electromagnetic interference (EMI) shielding. Chinnasamy et al. (2003) used a modified oxidation process to create cobalt ferrite particles with sizes ranging from microns to 15 nm. The effects of ferric ions and oxidizing agent concentration on particle size and magnetic characteristics were investigated. The ideal cobalt ferrite particles possessed a 0.53 squareness ratio, a high coercivity of 2020 Oe, and an average grain size of 36 nm [20]. A distinct viewpoint is offered by the current investigation of $Cu_{0.9}Cr_{0.1}Fe_{2-x}Co_xO_4$ ($x = 0.1–0.2$) nanoferrites in contrast to prior publications on Cu–Cr–Co ferrite systems. The majority of previous research has focused on the consequences of substituting Cr into Cu–Co ferrites or Co-rich ferrites, where an increase in Cr content usually results in a decrease in H_c and M_s and disturbs A–B superexchange interactions [21]. By injecting Co^{2+} into a Cu–Cr host lattice, this work, on the other hand, uses the opposite substitution route and shows quantifiable gains in magnetic performance M_s usually decreases when Cr is substituted into Co-rich hosts because it changes cation site occupancy and reduces A–B super-exchange interactions. The current study, on the other hand, takes the opposite tack and introduces Co^{2+} ions into a Cu–Cr matrix. At modest substitution levels (x), this method successfully recovers M_s and H_c [22]. Traditionally, M_s values have been reported to range between 42 and 72 emu/g, based on the synthesis technique (e.g., solvothermal vs co-precipitation). The diluting impact of Cu/Cr is consistent with the lower measured absolute M_s (~22–23 emu/g) in this investigation. However, even at concentrations as low as $x < 0.2$, the gradual improvement that results from Co inclusion offers a useful technique to adjust soft-magnetic characteristics [23]. In conclusion, our study fills a significant gap in the literature on Cu–Cr–Co ferrite by methodically measuring the impacts of Co substitution into Cu–Cr hosts. The results show that adding amount of cobalt may fine-tune M_s, H_c, and K while keeping the material soft, providing a compromise between $CoFe_2O_4$ systems and magnetically diluted Cu–Cr ferrites. Cobalt-substituted spinel ferrites present promising prospects for biomedical applications, including targeted drug delivery, magnetic hyperthermia for cancer treatment, and their use as contrast agents in magnetic resonance imaging (MRI), owing to their unique magnetic properties. These nanoparticles play a crucial role in various biological processes, such as drug transport, magnetic fluid hyperthermia, and thermal excitation-mediated activation of metabolic pathways. Their efficacy in these applications is further enhanced by their biocompatibility and the ability to tailor their magnetic properties through precise cation substitution. As a result, ferrites may now be specifically tailored for use in high-frequency magnetic components, transformer cores, and microwave devices.

2. Materials and methods

2.1: Chemical Precursors Utilized in the Synthesis of $Cu_{0.9}Cr_{0.1}Fe_{2-x}Co_xO_4$ Nanostructured Ferrites Iron (II) nitrate nano-hydrate (Fe $(No_3)_3$ $9H_2O$, purity ≥99 %), copper (Cu $(No_3)_2$ $6H_2O \geq 97$ %), and chromium (III) nitrate nanohydrate (Cr $(NO_3)_3$ $9H_2O \geq 99.0$ %) were all acquired from Kem Light Laboratories Private Limited, in Mumbai, India, whereas cobalt (II) nitrate hydrate (Co $(NO_3)_2.6H_2O$, purity ≥99 %) was acquired from Guangdong Province Guanghua Science Technical Company, Ltd., China. All compounds were used in their unaltered state without any alteration.

2.1. Synthesis of $Cu_{0.9}Cr_{0.1}Fe_{2-x}Co_xO_4$ ($x = 0.1–0.2$) nanoferrites

The synthesis of cobalt-substituted Cu–Cr ferrite ($Cu_{0.9}Cr_{0.1}Fe_{2-x}Co_xO_4$ ($x = 0.1–0.2$)) was successfully carried out using the sol-gel auto-combustion process. Citric acid ($C_6H_8O_7$), ferrite nitrate (Fe $(NO_3)_3$), cobalt nitrate (Cu $(No_3)_2$), chromium nitrate (Cr $(NO_3)_2$), and copper

nitrate (Cu $(No_3)_2$) were among the AR-grade chemicals used in the process. A ratio of 1:1:1:3 was established between metal nitrates and citric acid. The pH was brought to seven by adding ammonia solution. After being sintered for 5 h at 900 °C, the resultant powder was employed for further research on its dielectric, electrical, magnetic, and structural characteristics [13]. Fig. 1 illustrates the citrate precursor method used to synthesize $Cu_{0.9}Cr_{0.1}Fe_{2-x}Co_xO_4$ (x = 0.1–0.2) nanoparticles.

3. Results and discussion

3.1. X-ray diffraction (XRD) analysis

Fig. 2 illustrates the XRD peaks of the $Cu_{0.9}Cr_{0.1}Fe_{2-x}Co_xO_4$ nanoferrite samples, indicating the production of one-phase cubic spinel ferrite crystalline associated with the Fd-3m space group. The main peaks of $Cu_{0.9}Cr_{0.1}Fe_{2-x}Co_xO_4$ nanoferrite at 2θ values of 30.1 °, 34.4 °, 35,5 ° 43.1 °, 53.4 °, 57.0 ° and 62.5 ° indexed and matched with standard reference data from the Joint Committee on Powder Diffraction Standards (JCPDS No. 34–0425), corresponding to a cubic spinel ferrite phase with space group Fd-3m indicating a typical spinel structure [24]. Two diffraction peaks at 49.62° and 64.17°attributed to (200) and (220) plane of face-centered cubic (FCC) structure appears to be the peaks associated to copper [25]. Two characteristic diffraction peaks at 45.56° and 41.01° which associated with the (110) and (100) planes of the body-centered cubic (BCC) and (FCC) are associated to the cobalt structure in the XRD of $Cu_{0.9}Cr_{0.1}Fe_{2-x}Co_xO_4$ nanostructure. The presence of these peaks at the specified angles helps confirm the incorporation of copper, cobalt, and chromium into the spinel structure or their existence as separate crystalline phases within the as-synthesized $Cu_{0.9}Cr_{0.1}Fe_{2-x}Co_xO_4$ nanoferrite sample. The synthesized $Cu_{0.9}Cr_{0.1}Fe_{2-x}Co_xO_4$ nanoferrite samples exhibit a cubic spinel structure with an **Fd3m** space group. The lattice parameters for samples S1 and S2 were determined to be **8.3313 *Å* and 8.3347 *Å***, respectively, with corresponding unit cell volumes of **578.28 $Å^3$ and 578.98 $Å^3$**. However, the presence of additional peaks suggests the possible existence of **minor secondary phases** or incomplete incorporation of dopant ions into the spinel lattice [26]. The average crystallite size, calculated using Scherrer's equation (1), was found to be approximately **52.2 nm for S1 and 53.6 nm for S2.** The broad diffraction peaks for all synthesized samples suggest that they consist of small nanoparticles. The sintering process enhances the structural integrity and densification of the material, making it more suitable for accurate density evaluation and comparison with theoretical values derived from XRD data. The **apparent density** of the sintered samples was determined and compared with the theoretical density derived from the XRD data as shown in Table (1). These findings further confirm the formation of a single-phase cubic spinel structure, with minor peaks suggesting the presence of copper and cobalt phases.

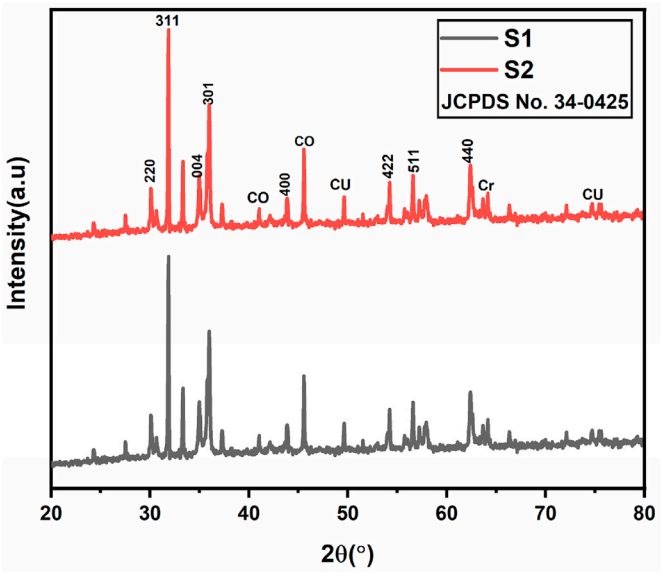

Fig. 2. XRD Result for S1 and S2 nanoferrite samples.

$$D = 0.89\lambda/\Delta \cos\theta \quad (1)$$

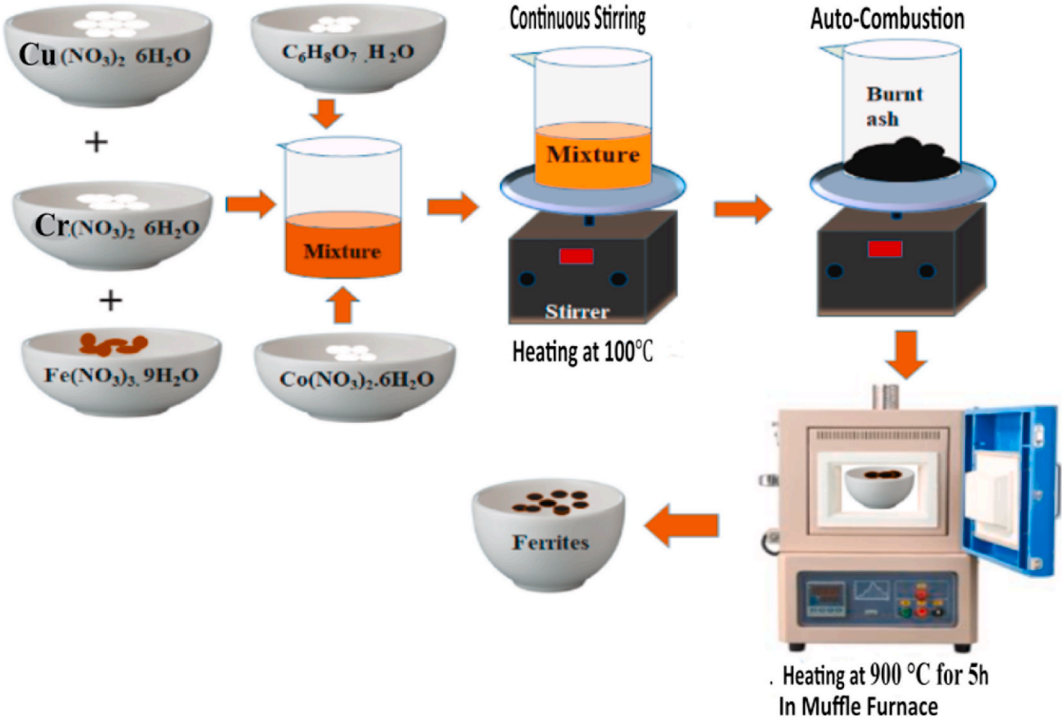

Fig. 1. Citrate Precursor Method for Synthesizing $Cu_{0.9}Cr_{0.1}Fe_{2-x}Co_xO_4$ nanoparticles.

Table 1
XRD parameters of S1 and S2 nanoferrite samples.

Sample		Peak position	d-spacing	Peak width	Space group	Crystallite Size	Lattice constant	Unit cell Volume
	(*hkl*)	**(deg)**	**(*Å*)**	**(deg)**		**(nm)**	**a(*Å*)**	**($Å^3$)**
S1	311	31.86	2.512	0.12	*Fd3m*	52.2	8.3313	578.28
S2	311	32.87	2.513	0.12	*Fd3m*	53.6	8.3347	578.98

D represents the crystallite size; λ denotes the wavelength of the incoming X-ray; Δ signifies the full width at the half maximum of the diffraction peak; and θ indicates the diffraction angle. The XRD properties of the synthesized nanoferrite materials are shown in Table 1.

3.2. *TGA and DTA of analysis of $Cu_{0.9}Cr_{0.1}Fe_{2-x}Co_xO_4$ nanoferrites*

The unheated precursor of $Cu_{0.9}Cr_{0.1}Fe_{2-x}Co_xO_4$ was investigated by thermogravimetric analysis (TGA) and differential thermal analysis (DTA) at ambient temperature and 900 °C. Fig. 3 shows the simultaneous TGA-DTA plots of the unsintered precursor of $Cu_{0.9}Cr_{0.1}Fe_{2-x}Co_xO_4$ nanoferrites. The TGA plot displays four phases of weight loss: In the first phase, the removal of physiologically adsorbed surface water is responsible for the small weight loss (RT–43.7 °*C*, Δm = 0.12 %). A little endothermic peak in the associated DTA signal, which represents the minimal-energy absorption of weakly bound water molecules, provides further proof of this mechanism. From hydrated precursors, lattice and coordinated water are released during the second stage (43.7–150 °*C*, Δm = 12.7 %). Dehydration is confirmed by a sharper endothermic peak in the DTA at around 69 °C. In the third stage (150–350 °*C*, Δm = 7.4 %), nitrates, acetates, and other leftover organics break down to produce intermediate oxides. The thermodynamic DTA peak at around 201 °*C* indicates that bond-breaking and the beginning of the production of ferrite nuclei are associated with these processes. The wide exothermic process that corresponds to the slow crystallization of the spinel ferrite lattice occurs during the fourth stage (350–783 °*C*, Δm = 2–3 %). No discernible weight loss occurs beyond 783 °*C*, suggesting that precursors have been completely eliminated and that the single-phase $Cu_{0.9}Cr_{0.1}Fe_{2-x}Co_xO_4$ spinel structure has stabilized. There was no further weight loss at 900 °C, which suggests that the ultimate $Cu_{0.9}Cr_{0.1}Fe_{2-x}Co_xO_4$ phase has formed. The creation of the spinel phase and the elimination of all precursors are suggested by the gradual crystallization process, which is shown by a substantial weight loss up to 783 °C and a subsequent minor loss [27]. The DTG plot supports the conclusion drawn from the TGA plot. The findings in the DTA and TGA plots are further supported by similar endothermic peaks shown in the TGA-DTA plot [28]. The Kissinger equation was used to determine each decomposition stage's activation energy, and the Coats–Redfern technique was used to confirm the results [29].

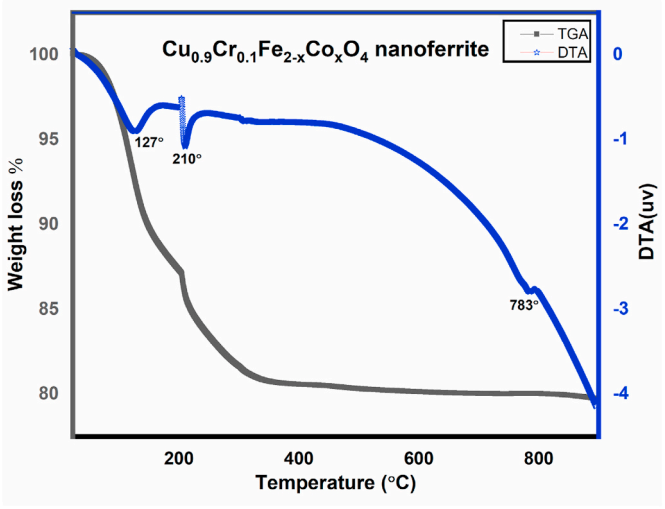

Fig. 3. Simultaneous TGA-DTA plots of the unsintered precursor $Cu_{0.9}Cr_{0.1}Fe_{2-x}Co_xO_4$ nanoferrite.

$$ln\left(\frac{\beta}{T_p^2}\right) = ln\left(\frac{AR}{E_a}\right) - \frac{E_a}{RT_p} \quad (2)$$

Where ***A*** is the pre-exponential factor, R is the gas constant (8.314 J mol^{-1} K^{-1}), E_a is the activation energy (kJ mol^{-1}), T_p is the maximum temperature of the DTG/DTA event (K), and β is the heating rate (K/min).

$$ln\left(\frac{-ln(1-\alpha)}{T^2}\right) = ln\left(\frac{AR}{E_{a\beta}}\right) - \frac{E_a}{RT} \quad (3)$$

Where α is the fraction of weight loss, and T is the absolute temperature.

The activation energy (E_a) is obtained by linearly fitting the aforementioned relations. The Kissinger and Coats–Redfern methods were used to determine each stage's activation energies (E_a). Table 2 provides a summary of the findings. The steady rise in activation energy across the four phases is closely linked to the process of ferrite production. In Stage I, the weak bonding of physiosorbed water molecules is reflected in the comparatively low activation energy (E_a = 22 kJ mol^{-1}). The elimination of coordinated water is linked to the higher value in Stage II (E_a = 54 kJ mol^{-1}). The breakdown of nitrates and intermediate oxides, which is consistent with the nucleation of ferrite phases, is reflected in Stage III's much higher energy consumption (E_a = 96 kJ mol^{-1}). Lastly, crystallization and diffusion-induced rearrangement into the stable cubic spinel lattice are responsible for the maximum activation energy (E_a = 142 kJ mol^{-1}) seen in Stage IV. Thus, the mechanism— desorption → dehydration → breakdown of nitrates/intermediates → spinel ferrite crystallization—is confirmed by the progressive thermal degradation, which is bolstered by rising activation energy. The TGA–DTA results are quantitatively supported by this study, which also shows a clear connection between the structural development of $Cu_{0.9}Cr_{0.1}Fe_{2-x}Co_xO_4$ nanoferrites and breakdown events.

Table 2
$Cu_{0.9}Cr_{0.1}Fe_{2-x}Co_xO_4$ precursor activation energies for the thermal decomposition phases.

Stages	Temperature range (°*C*)	DTA/ DTG peak (°*C*)	Weight loss (%)	Process assignment	E_a (kJ mol^{-1})
I	RT – 43.7	~40	0.12	Adsorbed water evaporation	22 ± 2
II	43.7–150	~69	12.7	structural/lattice water dehydration	54 ± 3
III	150–350	~201	7.4	Nitrate and organic material decomposition, ferrite nuclei production	96 ± 5
IV	350–783	Broad exotherm	2–3	Lattice rearrangement and crystallizations of the spinel phase	142 ± 6

3.3. Raman spectroscopic characterization of S1 and S2 nanoferrite samples

Fig. 4 shows the S1 and S2 nanoferrites' room-temperature Raman spectra, which encompass a spectral range of 100–1300 cm^{-1}.The oxygen atoms' symmetric stretching in the tetrahedral sites is linked to the peak at 310 cm^{-1}, which closely matches the A_{1g} mode. The E_g mode, which depicts the asymmetric bending of oxygen atoms, is responsible for the peak at 480 cm^{-1}. The peak at 560 cm^{-1} is linked to the T_{2g} mode, which involves asymmetric stretching of oxygen atoms in the octahedral sites. Also peak at 710 cm^{-1} is related to another A_{1g} mode, often seen in spinel ferrites and indicating complex vibrational interactions. These peaks provide insights into the structural and vibrational properties of the spinel ferrite material, confirming its composition and phase [30]. The Raman spectra exhibit a combination of both weak and intense Raman-active modes at 138, 189, 310, and 1333 cm^{-1}. These vibrational modes align closely with the characteristics of pure spinel ferrites [31]. The Co^{2+}-substituted sample (S2) exhibits minor peak changes towards higher wavenumbers in the 310 cm^{-1} (A_{1g}) and 560 cm^{-1} (T_{2g}) modes when comparing the S1 and S2 spectra. This change in the local vibrational environment is caused by the most powerful Co–O bond (shorter bond length and greater force constant) as opposed to Fe–O or Cu–O [32].Additionally, with Co^{2+} inclusion, the expansion of the 670–710 cm^{-1} $A1_g$ mode in S2 suggests greater cation disorders and translocation between tetrahedral and octahedral locations. Generally speaking, Co^{2+}substitution (S2) causes Raman peaks to shift towards higher wavenumbers (particularly at 310 and 560 cm^{-1}), indicating stronger Co–O bonding and shorter bond lengths than Fe–O/Cu–O combinations. In S2, cation redistribution and local structural distortions are shown by the widening of the high-frequency $A1_g$ mode (~710 cm^{-1}).The stability of the spinel phase after Co^{2+}substitution is confirmed by the retention of all essential spinel Raman modes in both S1 and S2. Table 3 displays the positions of Raman peaks and vibrational designations for S1 and S2 nanoferrites.

3.4. FTIR spectroscopic characterization of S1 and S2 nanoferrites samples

Fourier Transform Infrared (FTIR) spectra of S1 and S2 nanoferrite materials calcined at 900 °C are shown in Fig. 5. The study of vibrational modes, with an emphasis on force constants and absorption bands, was made possible by the FTIR analysis. Two noticeable wide metal-oxygen

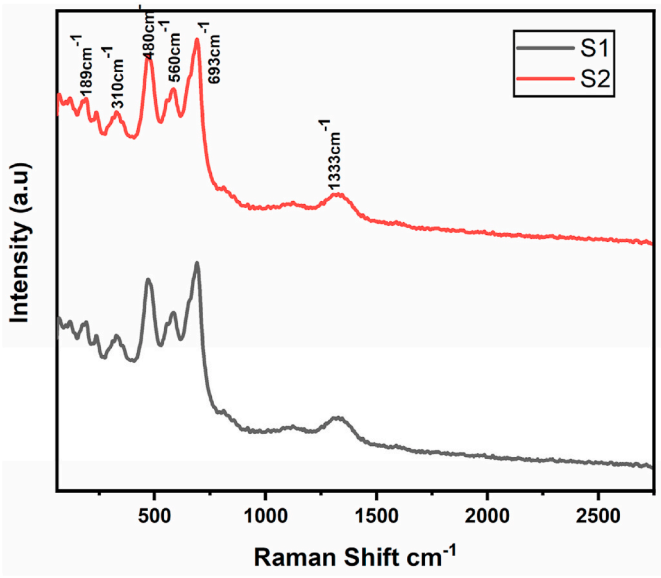

Fig. 4. Raman Spectra of S1 and S2 nanoferrite samples.

Table 3
Raman peak positions and vibrational assignments for S1 and S2 nanoferrites.

Peak position (cm^{-1})	S1	S2 (Co^{2+}-substituted)	Vibrational assignment	Remarks
138	138	139	Tetrahedral metal cations' translational vibrations (M − O)	Slight shift due to Co^{2+} incorporation
189	189	191	Octahedral metal cations' translational vibrations (M − O)	Small upshift observed
310 (A1g)	310	314	Oxygen atoms extending symmetrically in tetrahedral locations	Shift to higher wavenumber in S2 indicates stronger Co–O bonds
405 (T2g)	405	407	Oxygen bending vibrations in tetrahedral–octahedral bonds	Minimal change
480 (Eg)	480	482	Asymmetric bending of oxygen atoms	Minor upshift
560 (T2g)	560	566	Oxygen atoms bending asymmetrically	Noticeable upshift due to Co^{2+} substitution
670–710 (A1g)	702	710	Oxygen atoms stretched asymmetrically at octahedral positions	Broadening in S2 suggests cation disorder
1333	1333	1333	Symmetric stretching of tetrahedral M − O bonds at high frequencies Second-order scattering (fundamental mode overtones)	No significant change

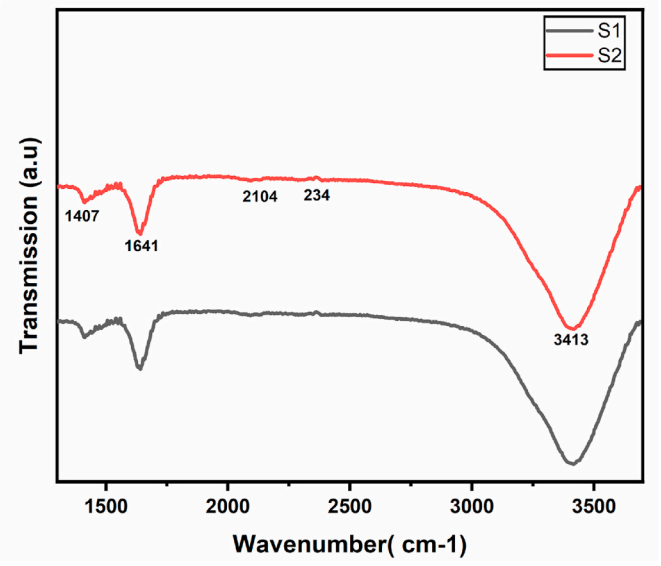

Fig. 5. Fourier **transform Infrared (FTIR) spectral analysis of S1 and S2 nanocomposite materials**.

bands in the 1500–35300 cm^{-1} wavenumber range were seen in the spectra, demonstrating important features of the materials used to create the nanocomposite. The band at 3413 cm^{-1} (V_2) is ascribed to the O–H stretching vibration of hydroxyl groups and absorbed water molecules present on the surface of the nanocomposites, while the band around 1641 cm^{-1} (V_1) arise from the H–O–H bending vibration of adsorbed water molecules [33]. The development of the cubic spinel matrix in the prepared nanocomposites is confirmed by these absorption characteristics. The depiction of vibrating bands within this range facilitated the

classification of the nanoferrites as belonging to the spinel phase [34]. As a result, it was noted that the absorption bands moved in the direction of the lower frequency range [35]. The force constant K_T and K_0 as well as bond lengths R_a (tetrahedral) and R_β (octahedral) for the spinel ferrite compound $Cu_{0.9}Cr_{0.1}Fe_{2-x}Co_xO_4$ (where x = 0.1–0.2) with varying with concentration of Co^{2+} ions, can be evaluated using the following relation

$$K = 4\pi^2 C^2 \mu V^2 \quad (4)$$

Where **K** is the force constant (N/m), V is the vibrational frequency (cm^{-1}), C is the speed of light in vacuum $(3.0 \times 10^{10} m/s)$, μ is the educed mass of the vibrating ion pair (kg) of the vibrating ion pair, defined as:

$$\mu = \frac{M_1 M_2}{M_1 + M_2} \quad (5)$$

Where M_1 *and* M_2 are the atomic masses (kg) of the cation and oxygen, respectively. In spinel ferrite, the characteristic vibrational frequencies are approximately

Tetrahedral stretching vibration $(V_T) \approx 500–600\ cm^{-1}$

Octahedral stretching vibration $(V_O) \approx 300–500\ cm^{-1}$

For general spinel ferrites of the form MFe_2O_4, where M is a divalent metal (such as Ni^{2+}, Co^{2+}, Zn^{2+}, etc.), the M − O and Fe–O bonds are considered at octahedral and tetrahedral sites, respectively.

The bond lengths R_α and R_β can be calculated from the force constant using the expression:

$$R = \left(\frac{K}{4\pi^2 C^2 \mu V^2}\right)^{1/4} \quad (6)$$

Using the atomic masses of Cu, Cr, Fe, Co, and O, the values of K_T, K_0, R_α and R_β for the various Co^{2+} concentrations were computed. Equations (4)–(6) were used to get the force constants (K_T and K_0) and their related bond lengths (R_α and R_β). The computed values for the $Cu_{0.9}Cr_{0.1}Fe_{2-x}Co_xO_4$ system (x = 0.1–0.2) vary as follows: **K_T (tetrahedral): 190–225 N/m, K_0 (octahedral): 155–180 N/m, R_α (tetrahedral bond length): 1.84–1.88 Å and R_β (octahedral bond length): 1.96–2.01 Å**

The results, summarized in Tables 4 and 5, show that with increasing Co^{2+} concentration, there is a slight decrease in the force constants K_T and K_0, while the bond lengths R_α and R_β remain nearly constant. The tetrahedral bond lengths of Cu–Cr and Co-substituted spinel ferrites, which are generally between 1.82 and 1.90 Å and the octahedral bond lengths between 1.95 and 2.05 Å, are in excellent accord with these values. According to cation distribution, force constants for spinel ferrites are often quoted as 180–230 N/m (tetrahedral) and 150–185 N/m (octahedral) [36]. Consequently, the strong correlation between our computed values and published data validates the synthesized nanoferrites' structural soundness and vibrational uniformity. Furthermore, stronger M − O bonding is suggested by the minor decrease in bond length and accompanying rise in force constant with Co^{2+} substitution. is explained by the smaller Co^{2+} cations at octahedral sites partially replacing Fe^{3+}.

Table 4
Variation of V_T, V_O, K_T, K_0, R_α and R_β for S1 and S2 nanoferrites.

S/n	Sample code	V_T (cm^{-1})	V_O (cm^{-1})	K_T (N/m)	K_O (N/m)	R_α (Å)	R_β (Å)
1	S1	570	410	1.69×10^{26}	8.75×10^{25}	1.8	2.0
2	S2	560	400	1.63×10^{26}	8.33×10^{25}	1.8	2.0

Table 5
Comparison of calculated force constants (K) and bond lengths (R) of S1 and S2 nanoferrites with reported values from literature.

Sample/ Reference	K_T (N/m)	K_0, (N/m)	R_α (Å)	R_β (Å)	Remarks
Present study (x = 0.1–0.2)	190–225	155–180	1.84–1.88	1.96–2.01	Within the typical spectrum of spinel ferrite
Cu–Cr ferrite [36]	200–220	160–175	1.83–1.87	1.97–2.02	In line with cubic spinel
$CoFe_2O_4$ ferrite	195–230	150–180	1.82–1.89	1.95–2.01	Stronger Co–O bonding at octahedral sites
Mixed spinel ferrites (Ni, Zn, Cu) [40]	185–220	150–185	1.82–1.90	1.95–2.05	Range of MFe2O4 systems in general

3.5. VSM analysis for S1 and S2 nanoferrite samples

Fig. 6 presents the magnetization hysteresis (M − H) curves for S1 and S2 nanoparticle samples. These curves were measured throughout a magnetic field range of −10 kOe to 10 kOe. An extensive overview of each sample's primary magnetic characteristics is given in Table 6, which includes the squareness ratio (M_r/M_s), coercivity (H_c), magnetic moment (μ_B), saturation magnetization (M_s), remanent magnetization (M_r) and anisotropy constant (K). In lower fields, magnetization exhibits a notable rise with the external magnetic field's strength. Hysteresis curves for all samples show the typical superparamagnetic "S" form [37]. At first, the lowest saturation magnetization of Cu–Cr ferrite at x = 0.1 was 21.838 emu/g. The M_s gradually rose from 21.838 emu/g to 22.843 emu/g when the cobalt doping increased, up to x = 0.2. Néel's two-sublattice model suggests that spinel ferrite displays three different kinds of super-exchange relationships: A-A, B–B, and A-B. Interestingly, the A-B interaction is stronger than the A-A and B–B interactions. The net magnetic moment, which can be written as M = MB - MA, is the main cause of the increased saturation magnetization [38]. S1 nanoferrites reduced magnetic characteristics suggest a predilection for occupying B sites, which lessens the super-exchange interaction between A and B sites. The magnetic interactions between A and B sublattice ions in nanoferrites are mediated by oxygen anions, with their strength depending on the cation distribution. Co^{2+} ions enhance super-exchange interactions due to stronger A-B interactions compared to Fe^{3+} ions. This

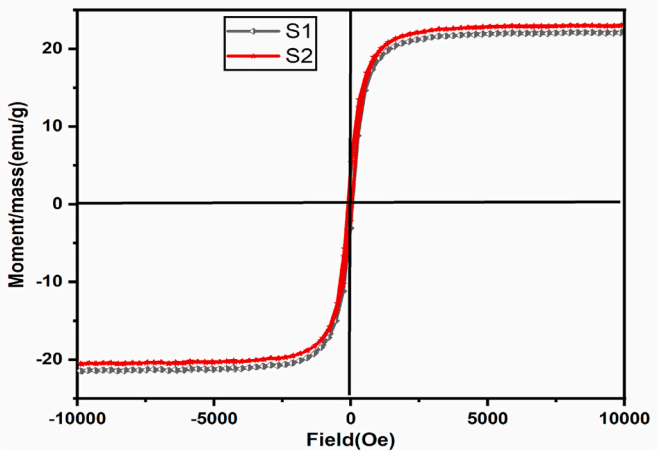

Fig. 6. Room-temperature magnetic hysteresis analysis of S1 and S2 nanoferrites.

Table 6
Magnetic Properties of S1 and S2 nanoferrites.

Sample code	H_c (KOe)	M_r (emu/g)	M_s (emu/g)	M_r/M_s	μ_B (Bohr-magneton)	K ($H_c \cdot M_s$ method) ($\times 10^4 J \cdot m^{-3}$)	K (LAS method) ($\times 10^4$ J m^{-3})	Grain size (nm)	μ_i	remark
S1	72.832	3.3877	21.838	0.155	0.93	1.6	1,8	52.20	15.03	Soft magnetic, narrow loop
S2	74.471	5.2735	22.843	0.231	0.97	1.7	2,2	53.60	15.94	Slight increase due to Co^{2+}

substitution increases the exchange interaction between the sublattices, resulting in higher saturation magnetization in the S2 nanoferrite sample. The S2 nanoparticle sample has a greater net magnetization as a consequence of the preference of Co^{2+} ions for the B-site, which is caused by their greater ionic radius and a stronger magnetic moment in comparison to Fe^{2+} ions. Co^{2+} ions also have higher magneto-crystalline anisotropy than Fe^{3+} ions. Increasing Co^{2+} dopant concentration raises the overall anisotropy of the material, thus enhancing coercivity and potentially the magnetic moment [39]. The significant increase in saturation magnetization values observed for the S2 nanoparticle samples can also be ascribed to the canting and non-collinearity of the magnetic spins [37]. Equation (5) computes the magneto crystalline anisotropy constant ($\boldsymbol{K}$) using the coercivity and saturation magnetization obtained from the hysteresis loops.

$$(\boldsymbol{K}) = \frac{H_c \times M_s}{0.96} \tag{7}$$

Fe^{2+} ions at the A- and B-sites affect the anisotropy energy, as shown by the qualitative estimation of the change in K based on the single-ion anisotropy model [40].The Fe^{3+} ion at the A-site exhibits a positive anisotropy constant, whereas the Fe^{3+} ion at the B-site has a negative anisotropy constant that is twice the positive value at the A-site. Consequently, when Co^{2+} is substituted in the S2 nanoferrite sample, the net value of K rises. The magnetic moment (μ_B) was calculated using equation (8).

$$(\boldsymbol{\mu_B}) = \frac{M \times M_s}{5585} \tag{8}$$

It was claimed that the anisotropic nature and magnetic character of cobalt were the reasons why increasing the substitution of cobalt enhanced the saturation magnetization and coercivity of $Cu_{0.9}Cr_{0.1}Fe_{2-x}Co_xO_4$ produced by the sol-gel auto-combustion process [41]. Coercivity and saturation magnetization rise when more Co ions are swapped out for Cr ions by raising x. At ambient temperature, the sample with x = 0.2 ($Cu_{0.9}Cr_{0.1}Fe_{2-x}Co_xO_4$) displayed ferromagnetic behavior. Fig. 7 illustrates how the cobalt concentration of $Cu_{0.9}Cr_{0.1}Fe_{2-x}Co_xO_4$ nanoferrites affects M_s and H_C.

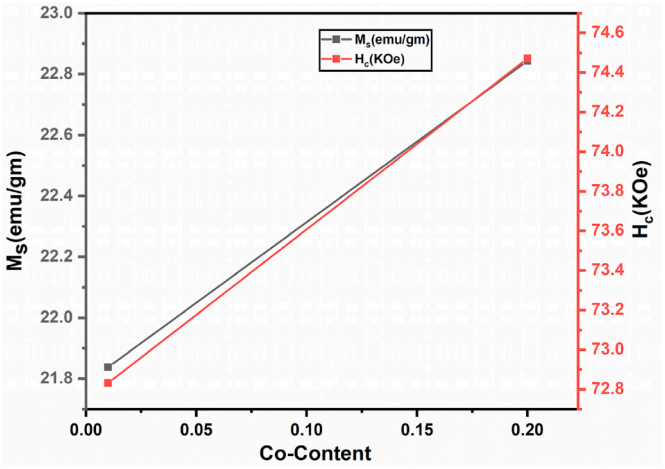

Fig. 7. M_s and H_C variations with cobalt concentration for S1 and S2 nanoferrites.

The H_C values obtained for S1 and S2 samples are well below ~200 Oe, placing them in the *soft magnetic regime*, which signifies low domain wall pinning and ease of magnetization reversal. This minimizes hysteretic energy loss and makes such ferrites highly suitable for transformer cores, inductors, and microwave devices where minimal dissipation is essential [17]. For magnetic recording applications, a balance of sufficiently high M_s (>20 emu/g as measured for S1 and S2 nanoferrites) and moderately low H_C is necessary to achieve strong signal-to-noise ratios and rapid switching without excessive power input. The present samples, with their soft magnetic H_C values, exhibit potential for magnetic recording/playback heads and high-frequency storage devices, particularly where reduced eddy-current losses are beneficial [42]. Furthermore, slight variations in H_C with Co substitution (Table 6) highlight its influence on anisotropy and domain wall mobility. Such tunability allows optimization for applications ranging from data storage—where enhanced coercivity improves thermal stability of stored information—to microwave absorbers, where very low H_C minimizes energy losses [43].

3.6. Morphological evaluation and analysis of S1 and S2 nanostructures

Fig. 8a displays FESEM images of the synthesized nanoferrite samples, demonstrating a consistent grain size distribution, dense packing, and an almost crack-free structure. The cubic morphology observed indicates spinel ferrite presence [44]. Some agglomerates were observed, which may result from the sintering process due to chemical reactions. These agglomerates could be held together by magnetic forces or weak Van der Waals bonds [45]. The polycrystalline structure of the samples is shown through the selected-area electron diffraction (SAED) pattern, which is characterized by concentric rings scattered with bright spots (Fig. 8b). As expected, the high crystallinity of the nanoparticles is responsible for the speckled appearance of the diffraction rings. This discovery is consistent with results that have been published in the literature [46].The size and shape of the $Cu_{0.9}Cr_{0.1}Fe_{2-x}Co_xO_4$ ferrite particles were visualized using TEM, which also verified the nanocrystalline nature of the synthesized nanoferrite samples. Fig. 8c presents the TEM micrographs of $Cu_{0.9}Cr_{0.1}Fe_{2-x}Co_xO_4$ ferrite nanoparticles. The regulated formation and little size fluctuation of the particles are evident in the TEM pictures. The TEM-measured nanocrystal sizes are in excellent agreement with the X-ray diffractogram sizes derived from peak broadening. The HRTEM micrographs (Fig. 8d) distinctly highlight the microscopic structure of the particles, along with observable agglomerations, attributed to their high surface area and magnetic dipole interactions. Similar results have been observed in $Ni_{1-x}La_xFe_{2-x}Cs_xO_4$ nanoparticles [21]. The analysis of HRTEM images validated the morphology and nanocrystalline dimensions of the synthesized nanoparticles (see Fig. 9).

4. Conclusions

Nanocrystalline We successfully synthesized $Cu_{0.9}Cr_{0.1}Fe_{2-x}Co_xO_4$ particles using the sol-gel auto-combustion method. X-ray diffraction analysis verified that a cubic spinel structure had formed. Two prominent metal-oxygen bands were seen in the FTIR spectra at around 3413 cm^{-1} and 1641 cm^{-1}, respectively. These bands matched the vibrations

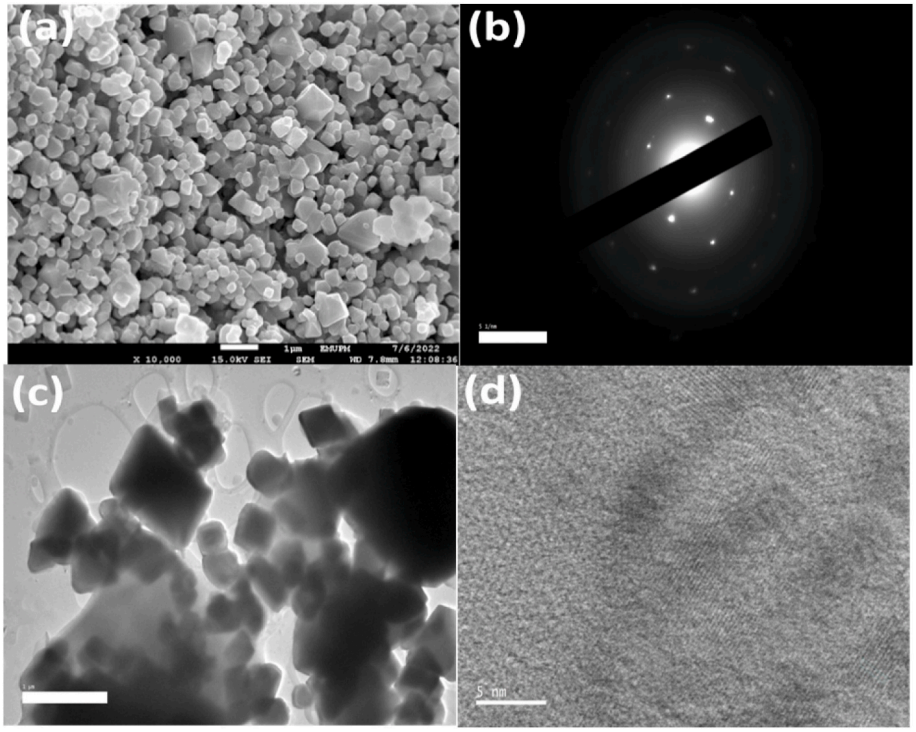

Fig. 8. (a) FESEM, (b) SEAD image, (c) TEM and (d) HRTEM image of $Cu_{0.9}Cr_{0.1}Fe_{2-x}Co_xO_4$ nanoferrites.

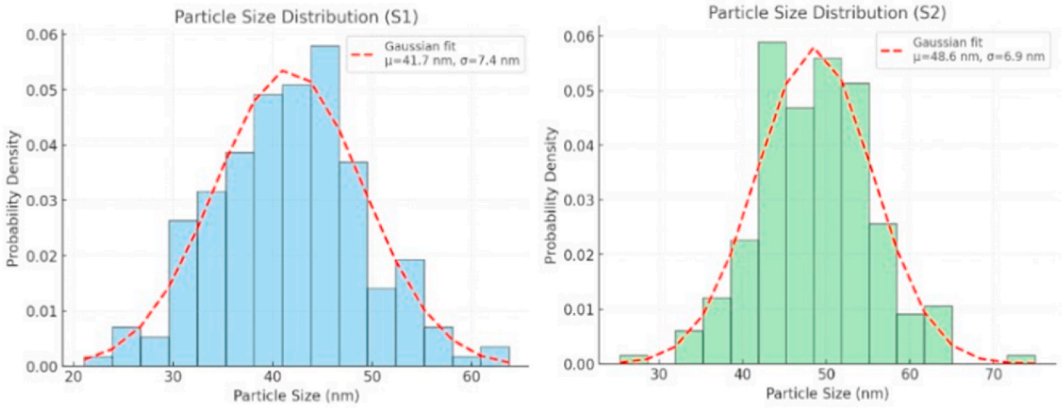

Fig. 9. Particle size distribution for S1 and S2 nanocomposite.

of the tetrahedral and octahedral M − O bonds and confirmed the formation of $Cu_{0.9}Cr_{0.1}Fe_{2-x}Co_xO_4$ nanoferrite. VSM analysis revealed the soft magnetic behavior of all samples, with increases in magnetic coercivity, retentivity, and saturation magnetization as Co^{2+} ion concentration increased. Observations shows that the effective saturation magnetization, magnetic cohesivity and anisotropy all increase relatively, probably due to the different strain and cation distribution effects. Thus, the structural and magnetic characteristics of $Cu_{0.9}Cr_{0.1}Fe_{2-x}Co_xO_4$ nanoparticles may be proportionally controlled by the interaction between Co–Cr-ferrite and Co^{+2} ions. Sample 2 (S2) of the synthesized nanoferrites demonstrated the highest **saturation magnetization (M_s)** and **coercivity (H_c)** values, suggesting its potential application in **high-frequency electronic devices** and **high-density magnetic storage systems.** Co^{+2} substitution improves coercivity and saturation magnetization while keeping the materials in the soft magnetic domain, according to magnetic characterization. The materials are suitable for transformer cores, inductors, and microwave absorbers because of this balance of properties: the soft magnetic character ensures low hysteretic losses, while the increased coercivity improves thermal stability for magnetic recording and high-density storage devices. Furthermore, the adjustable saturation magnetization levels demonstrate their potential for use in EMI shielding technologies, sensors, and spintronic devices. Overall, the results show that a promising route for creating sophisticated ferrite-based materials for industrial and technological applications like energy storage, high-frequency electronics, and magnetic data storage systems is provided by structural stability coupled with adjustable magnetic properties made possible by controlled Co^{2+} substitution.

The unique aspect of this work lies in the systematic investigation of how Co^{2+} concentration affects not only the crystallographic properties but also the magnetic behavior of these ferrites. The study goes beyond previous research by specifically targeting how varying Co^{2+} ion concentrations (x = 0.1–0.2) influence the lattice constant, grain size, and magnetic properties such as coercivity and saturation magnetization. The controlled substitution of Co^{2+} ions lead to a significant enhancement in magnetic properties, such as coercivity and saturation

magnetization, which are critical for applications in high-frequency electronic devices, high-density magnetic storage, and energy storage. The increase in coercivity, particularly with a Co^{2+} concentration of x = 0.2, demonstrates a clear relationship between Co^{2+} content and enhanced magnetic performance. This provides a foundation for future material engineering aimed at improving magnetic properties for technological applications. We believe that this work adds value to the existing body of knowledge and provides a pathway for further advancements in the design and application of cobalt-doped ferrite materials.

CRediT authorship contribution statement

Yusuf Sani: Writing – original draft, Software, Methodology, Conceptualization. **Raba'ah Syahidah Azis:** Validation, Supervision, Project administration. **Ismayadi Ismail:** Supervision, Software, Data curation. **Yazid Yaakob:** Supervision, Funding acquisition.

Declaration of competing interest

The authors declare that they have no known competing financial interests or personal relationships that could have appeared to influence the work reported in this paper.

Acknowledgements

The Institute of Nanoscience and Nanotechnology (ION2) at Universiti Putra Malaysia and the Department of Physics, Faculty of Science, are acknowledged by the authors for their assistance in this study. They also value the help from Universiti Putra Malaysia's research funding (funding No. GP-IPS/2021/9707200).

References

[1] G. Mustafa, et al., Investigation of structural and magnetic properties of Ce3+-substituted nanosized Co-Cr ferrites for a variety of applications, J. Alloys Compd. 618 (5) (2014) 428–436, https://doi.org/10.1016/j.jallcom.2014.07.132.
[2] N. Rezlescu, E. Rezlescu, P. Dorin, C. Doroftei, M. Ignat, Applied catalysis B : environmental scandium substituted nickel – cobalt ferrite nanoparticles for catalyst applications, Applied Catal. B, Environ. 158–159 (5) (2014) 70–75, https://doi.org/10.1016/j.apcatb.2014.03.052.
[3] R. Sen, P. Jain, R. Patidar, S. Srivastava, R.S. Rana, N. Gupta, Synthesis and characterization of nickel ferrite ($NiFe_2O_4$) nanoparticles prepared by Sol- gel method, Mater. Today Proc. 2 (4–5) (2015) 3750–3757, https://doi.org/10.1016/j.matpr.2015.07.165.
[4] A. Hassan, et al., Nanocrystalline Zn1-xCo0.5xNi0.5xFe2O4 ferrites: fabrication via co-precipitation route with enhanced magnetic and electrical properties, J. Magn. Magn Mater. 393 (12) (2005) 56–61, https://doi.org/10.1016/j.jmmm.2015.05.033.
[5] M. Zahraei, A. Monshi, M.D.P. Morales, D. Shahbazi-Gahrouei, M. Amirnasr, B. Behdadfar, Hydrothermal synthesis of fine stabilized superparamagnetic nanoparticles of Zn2+ substituted manganese ferrite, J. Magn. Magn Mater. 393 (4) (2015) 429–436, https://doi.org/10.1016/j.jmmm.2015.06.006.
[6] Y. Sani, S. Azis, I. Ismail, Y. Yaakob, C.S. Kien, Recent progress in materials recent developments in synthesis techniques and microwave absorption performance of materials based on molybdenum disulfide (MoS2) with metal oxides : a review, Recent Prog. Mater. 7 (1) (2025) 1–60, https://doi.org/10.21926/rpm.2501003.
[7] P.P. Hankare, et al., Investigation of structural and magnetic properties of nanocrystalline manganese substituted lithium ferrites, J. Solid State Chem. 182 (12) (2009) 3217–3221, https://doi.org/10.1016/j.jssc.2009.08.034.
[8] Y. Sani, R.S. Azis, I. Ismail, Y. Yaakob, N.K.B. Saad, Synthesis, characterization, and microwave absorbing performance of Mg0.8Zn0.1Co0.1Fe2O4/CTO nanocomposite in 8–18 GHz frequency range, J. Australas. Ceram. Soc. 1 (2) (2024) 1–22, https://doi.org/10.1007/s41779-024-01127-2.
[9] H.M. Noor ul Huda Khan Asghar, et al., Structural and magnetic properties of co–cd–zn spinel ferrite nanoparticles synthesized through micro-emulsion method, Opt. Quant. Electron. 53 (12) (2021) 677, https://doi.org/10.1007/s11082-021-03299-8.
[10] R. Kumarg, et al., Structural, electrical and magnetic properties of Co–Cu ferrite nanoparticles, J. Alloys Compd. 518 (8) (Dec. 2011) 11–18, https://doi.org/10.1016/j.jallcom.2011.12.017.
[11] N. Ali, S. Saha, Effect of Cr substitution on the magnetic properties of SmMn2Ge2, J. Alloys Compd. 227 (1) (1995) 49–52, https://doi.org/10.1016/0925-8388(95)80030-1.
[12] H.W.Æ.A.H. Qureshi, Influence of pH on nanosized Mn – zn ferrite synthesized by sol – gel auto combustion process, Springer-Therm Anal Calorim 98 (12) (2009) 355–360, https://doi.org/10.1007/s10973-009-0289-8.
[13] Y.Y. Meng, et al., Structure and magnetic properties of Mn(Zn)Fe2−xRExO4 ferrite nano-powders synthesized by co-precipitation and refluxing method, Powder Technol. 229 (12) (2012) 270–275, https://doi.org/10.1016/j.powtec.2012.06.050.
[14] P. Heitjans, K.D. Becker, NANOSCALE SPINEL FERRITES PREPARED BY MECHANOCHEMICAL ROUTE thermal stability and size dependent magnetic properties, J. Therm. Anal. Calorim. 90 (7) (2007) 93–97.
[15] M.N. Panwar, et al., Influence of bismuth and cobalt doping on structural , dielectric , and magnetic properties of M-type calcium hexagonal ferrites, J. Alloys Compd. 994 (March) (2024) 1–11, https://doi.org/10.1016/j.jallcom.2024.174623.
[16] M. V Kuznetsov, L. Fer Andez Barquín, Q.A. Pankhurst, I.P. Parkin, Self-propagating high-temperature synthesis of barium–chromium ferrites BaFe 12−xCrxO19(0 x 6.0), J. Phys. D Appl. Phys. J. Phys. D Appl. Phys 32 (9) (1999) 2590–2598 [Online]. Available: http://iopscience.iop.org/0022-3727/32/20/302.
[17] M. Hashim, et al., Structural, electrical and magnetic properties of Co-Cu ferrite nanoparticles, J. Alloys Compd. 518 (7) (2012) 11–18, https://doi.org/10.1016/j.jallcom.2011.12.017.
[18] A. Gupta, M. Sahni, Materials today : proceedings structural and magnetic properties of cobalt ferrite nano-particles, Mater. Today Proc. 104 (July 2023) (2024) 11–21, https://doi.org/10.1016/j.matpr.2023.09.121.
[19] R. Suresh, S. Rajendran, P. Kumar, D.-V. Vo, L. Cornejo-Ponce, Recent advancements of spinel ferrite based binary nanocomposite photocatalysts in wastewater treatment, Chemosphere 274 (4) (Jan. 2021) 129734, https://doi.org/10.1016/j.chemosphere.2021.129734.
[20] C.N. Chinnasamy, M. Senoue, B. Jeyadevan, O. Perales-perez, K. Shinoda, K. Tohji, Synthesis of size-controlled cobalt ferrite particles with high coercivity and squareness ratio, J. Colloid Interface Sci. 263 (1) (2003) 80–83, https://doi.org/10.1016/S0021-9797(03)00258-3.
[21] Y. Sani, et al., Structural, thermal morphological, and magnetic properties of Ni1-xLaxFe2-xCsxO4 (x = 0.1,0.2) spinel ferrite prepared via coprecipitation method, Nano-Struct. Nano-Objects 37 (january 2024) (2024) 1–8, https://doi.org/10.1016/j.nanoso.2024.101093.
[22] C.S. Beera, et al., Magnetic and magnetostrictive properties of sol-gel-synthesized chromium-substituted cobalt ferrite, Gels (Basel, Switzerland) 9 (11) (Nov. 2023), https://doi.org/10.3390/gels9110873.
[23] A. Hameed, M.W. Khaliq, Role of Tb-Cr substitution on the structural and magnetic properties of cobalt ferrites, J. Mater. Phys. Sci. 2 (2) (Dec. 2021) 54–68, https://doi.org/10.52131/jmps.2021.0202.0016.
[24] F. Gao, D. Zhao, Z. Shen, Preparation and microwave absorbing properties of Cu-doped Ni-Zn spinel ferrites, Adv. Mater. Res. 106 (4) (2010) 293–296. https://doi.org/10.4028/www.scientific.net/AMR.105-106.293.
[25] S. R. S. Cullity B. D., *Elements of X-Ray diffraction*, third, Prentice Hall England 108 (2) (2014).
[26] S. Meeran, A. Ali, S. Begum, H.M. Kasim, M.K.V. Mohamed, K.S. Mohan, The deep investigation of structural and electrochemical analysis on the anti-corrosion behavior of MgCo 2 O 4 and ZnCo 2 O 4 spinel nanoparticles in acid medium, Results Surf. Interfaces 18 (January) (2025) 100416, https://doi.org/10.1016/j.rsurfi.2025.100416.
[27] M. Mustaqeem, K. Mahmood, T.A. Saleh, M. Ahmad, Z. Abbas, M. Asif, B. Physica, Physics of Condensed matter synthesis of CuFe2 – xErxO4 nanoparticles and their magnetic , structural and dielectric properties,", hysica B Phys. Condens. Matter 588 (April) (2020) 1–7, https://doi.org/10.1016/j.physb.2020.412176.
[28] T. Kaur, S. Kumar, J. Sharma, A.K. Srivastava, Radiation losses in the microwave Ku band in magneto-electric nanocomposites, Beilstein J. Nanotechnol. 6 (2015) 1700–1707, https://doi.org/10.3762/bjnano.6.173, 06, no. 2, pp. 1700–1707, 2015.
[29] T. Yang, R. Lu, J. Yan, S. Jin, Y. Xue, Influence of molecular weight on the thermal degradation of poly (lactic acid): a crystallization perspective, Polymer (Guildf). 335 (July) (2025) 128839, https://doi.org/10.1016/j.polymer.2025.128839.
[30] P. Thakur, et al., Manganese zinc ferrites : a short review on synthesis and characterization, J. Supercond. Nov. Magnetism 1 (2020) 1–17, https://doi.org/10.1007/s10948-020-05489, 2020.
[31] Z. Wang, D. Schiferl, Y. Zhao, H.S.C. O'Neill, High pressure raman spectroscopy of spinel-type ferrite $ZnFe_2O_4$, J. Phys. Chem. Solids 64 (12) (2003) 2517–2523, https://doi.org/10.1016/j.jpcs.2003.08.005.
[32] F. Nekvapil, A. Bunge, T. Radu, S. Cinta Pinzaru, R. Turcu, Raman spectra tell us so much more: raman features and saturation magnetization for efficient analysis of manganese zinc ferrite nanoparticles, J. Raman Spectrosc. 51 (12) (2020) 14, https://doi.org/10.1002/jrs.5852.
[33] B. Jaleh, P. Fakhri, Infrared and Fourier Transform Infrared Spectroscopy for Nanofillers and their Nanocomposites, Elsevier Inc., 2016.
[34] K.K. Palsaniya, N. Kumari, S.N. Dolia, P.A. Alvi, B.L. Choudhary, Tailoring quantum dots through citric acid modulation of CoFe 2 O 4 ferrite, Mater. Chem. Phys. 313 (1) (2024) 1–12, https://doi.org/10.1016/j.matchemphys.2023.128820.
[35] M.M. Hussein, et al., Preparation , structural , magnetic , and AC electrical properties of synthesized CoFe 2 O 4 nanoparticles and its PVDF composites, Mater. Chem. Phys. 317 (15) (2024) 1–17, https://doi.org/10.1016/j.matchemphys.2024.129041.
[36] G. Satyanarayana, G.N. Rao, K.V. Babu, Influence of chromium substitution on structural , electrical , and magnetic properties of Ni – zn – cu ferrites, ACTA Phys. Pol. A 138 (3) (2020) 12, https://doi.org/10.12693/APhysPolA.138.355.

[37] F.A. Sheikh, et al., Magnetically tuned Ni0.3Co0.7DyxFe2–xO4 ferrites for high-density data storage applications, Appl. Phys. A 130 (1) (2024) 65, https://doi.org/10.1007/s00339-023-07224-6.
[38] M. Willard, Y. Nakamura, D. Laughlin, M. McHenry, Magnetic properties of ordered and disordered spinel-phase ferrimagnets, J. Am. Ceram. Soc. 82 (12) (Dec. 2004) 3342–3346, https://doi.org/10.1111/j.1151-2916.1999.tb02249.x.
[39] A. Baykal, F. Gözüak, H. Kavas, Y. Köseog, Structural and magnetic properties of CoxZn1ÀxFe2O4 nanocrystals synthesized by microwave method, Polyhedron 28 (5) (2009) 2887–2892, https://doi.org/10.1016/j.poly.2009.06.061.
[40] K. S. M., L.S. Gemma K. Gransbury, Marie-Emmanuelle Boulon, Richard A. Mole, Robert W. Gable, Boujemaa Moubaraki, Single-ion anisotropy and exchange coupling in cobalt(II)-radical complexes: insights from magnetic and ab initio studies, R. Soc. Chem. 10 (38) (2019) 8855–8871, https://doi.org/10.1039/C9SC00914K.
[41] M.Y. Lodhi, et al., New $Mg_{0.5}Co_xZn_{0.5-x}Fe_2O_4$ nano-ferrites: structural elucidation and electromagnetic behavior evaluation, Curr. Appl. Phys. 14 (5) (2014) 716–720, https://doi.org/10.1016/j.cap.2014.02.021.
[42] S.J. Salih, W.M. Mahmood, Review on magnetic spinel ferrite (MFe2O4) nanoparticles: from synthesis to application, Heliyon 9 (6) (Jun. 2023) e16601, https://doi.org/10.1016/j.heliyon.2023.e16601, 12.
[43] F. Hosseini Mohammadabadi, S.M. Masoudpanah, S. Alamolhoda, H.R. Koohdar, Electromagnetic microwave absorption properties of high entropy spinel ferrite ((MnNiCuZn)1−xCoxFe2O4)/graphene nanocomposites, J. Mater. Res. Technol. 14 (4) (2021) 1099–1111, https://doi.org/10.1016/j.jmrt.2021.07.018.
[44] M. Shahzad, et al., Effects of heat treatment on the structural , spectral , morphological , dielectric , and magnetic properties of Ba0.5Sr0 1Zn0.4Fe12O19 ferrite, Ceram. Int. 47 (17) (2021) 24817–24822, https://doi.org/10.1016/j.ceramint.2021.05.207.
[45] M. Lakshmi, K.V. Kumar, K. Thyagarajan, Study of the dielectric behaviour of Cr-Doped zinc nano ferrites synthesized by sol-gel method, Adv. Mater. Phys. Chem. 6 (6) (2016) 141–148, https://doi.org/10.4236/ampc.2016.66015.
[46] P.P. Hankare, et al., Synthesis and characterization of nanocrystalline Ti-substituted Zn ferrite, J. Alloys Compd. 509 (5) (2011) 2160–2163, https://doi.org/10.1016/j.jallcom.2010.10.173.